Magnetic and Gravity Surface Geometry Inverse Modelling of the TAG Active Mound

C. Galley[1], P. Lelièvre[2], A. Haroon[3], S. Graber[3], J. Jamieson[1], F. Szitkar[4], I. Yeo[5], C. Farquharson[1], S. Petersen[3], and R. Evans[6]

[1]Memorial University of Newfoundland

[2]Mount Allison University

[3]Helmholtz Centre for Ocean Research GEOMAR Kiel

[4]The Geological Survey of Norway

[5]National Oceanography Centre Southampton

[6]Woods Hole Oceanographic Institution

0000-0002-3401-0376

Corresponding author: Christopher Galley (cggalley@mun.ca)

Key Points:

- Seafloor massive sulfide deposits can be modelled in 3D by inverting seafloor magnetic and gravity data.
- Sparse drilling can be improved upon with geophysical inverse modelling to enhance 3D deposit models.
- An updated massive sulfide tonnage estimate was determined for the Trans-Atlantic Geotraverse active mound.

Abstract

Seafloor massive sulfide deposits form in remote environments, and the assessment of deposit size and composition through drilling is technically challenging and expensive. To aid the evaluation of the resource potential of seafloor massive sulfide deposits, three-dimensional inverse modelling of geophysical potential field data (magnetic and gravity) collected near the seafloor can be carried out to further enhance geologic models interpolated from sparse drilling. Here, we present inverse modelling results of magnetic and gravity data collected from the active mound at the Trans-Atlantic Geotraverse hydrothermal vent field, located at 26º08'N on the Mid-Atlantic Ridge, using autonomous underwater vehicle (AUV) and submersible surveying. Both minimum-structure and surface geometry inverse modelling methods were utilized. Through deposit-scale magnetic modelling, the outer extent of a chloritized alteration zone within the basalt host rock below the mound was resolved, providing an indication of the angle of the rising hydrothermal fluid and the depth and volume of seawater/hydrothermal mixing zone. The thickness of the massive sulfide mound was determined by modelling the gravity data, enabling the tonnage of the mound to be estimated at 2.17 +/- 0.44 Mt through this geophysics-based, non-invasive approach.

1 Introduction

Seafloor massive sulfide (SMS) deposits form at the seafloor at sites of high-temperature hydrothermal venting. These metal-rich deposits represent the modern equivalents of ancient volcanogenic massive sulfide (VMS) deposits, and serve as a potential future source for copper, gold, silver, zinc, and lead (Hannington et al., 2011). They form at or near the seafloor by the precipitation of sulfide minerals from metal-laden hydrothermal fluids, where the remote environment and hostile conditions make conventional deposit assessment methods such as drilling challenging and expensive.

The Trans-Atlantic Geotraverse (TAG) active mound is a hydrothermally active SMS deposit located on the hanging wall of a detachment fault at 26º08'N along the Mid-Atlantic Ridge (Fig. 1; Rona et al., 1993; Tivey et al., 2003). The TAG mound is composed primarily of massive sulfide and anhydrite (Petersen et al., 2000). Drilling of the active mound was conducted in 1994 as part of the Ocean Drilling Program (ODP) Leg 158, from which a mineralogical reconstruction of the active mound's massive sulfide and sulfate interior, silicified wallrock breccia, and chloritized basalt unit was created (Knott et al., 1998; Smith & Humphris, 1998). The deposit's outer most subseafloor alteration unit, the chloritized basalt, was intersected by three of the Leg 158 boreholes (TAG 1, 2b, and 4), but those boreholes did not penetrate deep enough to intersect the contact between the chloritized basalt and unaltered basalt. This chloritization of the seafloor is an alteration process that occurs as a result of the rising hydrothermal fluids mixing with the more magnesium rich local seawater at > 200°C (Galley & Koski, 1999; Humphris et al., 1998; Seyfried & Bischoff, 1981). Information regarding the depth and scale of the local seawater circulation into the TAG hydrothermal system could be derived from the geometry and size of the chloritized basalt unit.

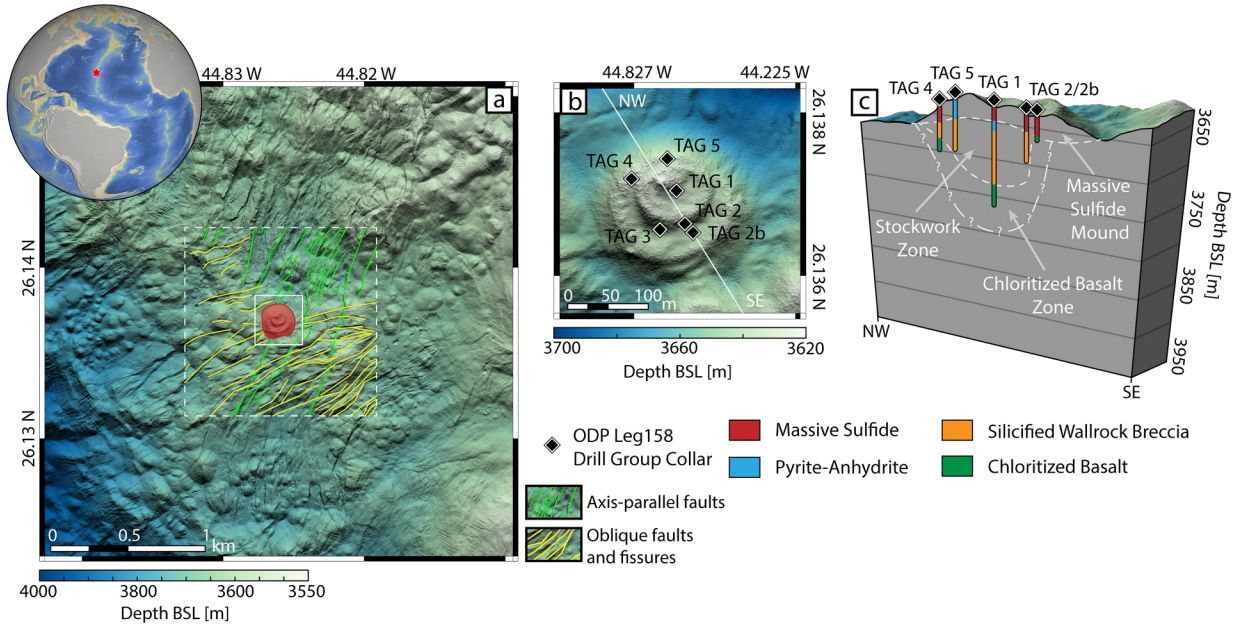

Figure 1. a) The bathymetric map of the study area. The regional inversion model's volume of interest is outlined with a dotted white line, whereas the volume of interest for the deposit scale inversion is outlined by a solid white line. Structural information is from Graber et al. (2020); **b)** Map of the TAG active mound showing locations of the ODP Leg 158 boreholes; **c)** borehole lithology logs from Knott et al. (1998) projected onto a NW/SE cross section (white line in b). Bathymetric data with 2 m resolution was collected in 2016 using the GEOMAR AUV *Abyss* (Petersen and Shipboard Scientific Party, 2016).

The rising hydrothermal fluids and their associated seafloor alteration have multiple effects on the physical properties of the crust. The hydrothermal fluids increase the rate of alteration of the titanomagnetite within the basalt to the less magnetic titanomaghemite, as well as increasing the rate of titanium dissolution from the titanomagnetites, making SMS deposits low magnetic anomalies both at the seafloor and deep into the crust (Szitkar et al., 2014; Wang et al., 2020). On the deposit scale all lithologic zones (i.e. the massive sulfide mound and the stockwork zone; Fig. 1c) within the chloritized basalt unit contain the lowest magnetic properties (Wang et al., 2020), with a secondary low extending down the length of the hydrothermal fluid upflow zone (Galley et al., 2020a). Despite the TAG mound being a homogeneous magnetic low, its massive sulfide mound unit can be distinguished from the other units by its anomalously high density (Evans, 1996; Ludwig et al., 1998), caused by its primary composition of massive sulfide (with a density of approximately 3.65 g/cm^3 compared to 2.4 g/cm^3 for basalt; Evans, 1996).

Investigations of the subseafloor structure of SMS deposits have been mainly driven by drilling. The sparse drilling at the TAG active mound has provided key information on the geometry (Humphris et al., 1995) and genesis of SMS and VMS deposits (You & Bickle, 1998), and has led to the TAG active mound model to be widely used as a representative for a generic SMS deposit (Galley et al., 2007). However, the geological interpretation of the TAG active mound was primarily two-dimensional (2D), with only one borehole (TAG 1) extending deep (approximately 120 m) into the deposit's core (Knott et al., 1998). The overall drilling was therefore not deep enough to determine the thickness of the chloritized basalt unit that underlies the silicified wallrock breccia zone, as the drillholes did not intersect the interface between chloritized and unaltered basalt. Additionally, to estimate the mound’s sulfide mineral tonnage, symmetry was assumed orthogonal to the 2D geologic interpretation (Hannington et al., 1998). This study expands on our previous knowledge of the geometry of subseafloor SMS hydrothermal alteration units by inverting for a 3D geophysical model of the chloritized basalt unit, as well as a 3D model of the deposit.

The two most commonly used methods for modelling magnetic data from SMS deposits are those of Parker & Huestis (1974) and Honsho et al. (2012), which both solve for a magnetization distribution. The distribution varies laterally, with no vertical changes and a fixed thickness to the magnetized crustal layer, typically 500 m (Szitkar & Dyment, 2015), but the thickness has also been defined by the Curie isotherm depth (Bouligand et al., 2020). Minimum-structure inverse modelling can be an effective alternative method to model the variations in physical properties around and within SMS deposits (Kowalczyk, 2011; Caratori Tontini et al., 2012; Galley, et al., 2020a). This modelling method uses a three-dimensional discretization of the crust, known as a mesh, and solves for the target physical property values inside each of the mesh's cells. Minimum-structure inverse modelling is robust, requiring little prior knowledge of the subsurface to construct a feasible geophysical model (Constable et al., 1987). Here, the minimum-structure inverse modelling uses the method as described in Galley et al. (2020a), which discretizes the crust using a tetrahedral mesh as to closely fit the variable bathymetry and solves for the effective magnetic susceptibility in each tetrahedral cell.

Minimum-structure inverse models are smooth by design and as such can have difficulty determining the locations of discrete or almost discrete boundaries between petrophysically contrasting lithological units. To further improve upon a subsurface physical property model, a surface geometry inversion (SGI) method can be used to solve for a wireframe model of an SMS deposit (Galley et al., 2020b). Our SGI method creates a wireframe surface model of rock unit contacts by inverting for the 3D position of the vertices that define the surface mesh. This is accomplished using first a Genetic Algorithm (GA) to find the model that best fits the data, followed by a Monte-Carlo Markov chain (MCMC) to calculate the model's uncertainty. Modelling SMS deposits as wireframe models creates geophysical models that are formatted similar to geological interpretations and allow for the volumes of alteration units to be easily calculated.

Previous geophysical models of the TAG active mound have included inverting magnetic data to study the lateral variations in magnetization at the deposit (Szitkar & Dyment, 2015; Tivey et al., 1993), as well as inverting controlled-source electromagnetic (CSEM) data to develop 2D conductivity cross-sections through the TAG mound (Gehrmann et al., 2019). The magnetization models have led to the lateral extents of the near-surface hydrothermal alteration to be mapped, allowing the deposit to be identified by a low magnetization anomaly that extends into the seafloor; however the models did not identify the vertical variations in the deposit's alteration. Gehrmann et al. (2019)'s CSEM inversions included two ~100 m thick cross-sectional models that passed orthogonally through the TAG active mound, allowing the high conductivity regions associated with massive sulfide mineralization to be identified. The relatively shallow depth of penetration of these CSEM models allows them to map the conductivity anomalies in the upper alteration units of the mound, but the smooth nature of the minimum-structure inversion models limits the model resolution and creates difficulties when trying to identify the thickness of the zone of mineralization.

With the incorporation of the Leg 158 drilling information, AUV magnetic data collected during the 2016 RV Meteor M127 cruise (Petersen and Shipboard Scientific Party, 2016) and seafloor gravity data collected in the Shinkai 6500 submersible (Evans, 1996), minimum-structure and SGI models are used to develop a new three-dimensional geological model of the TAG active mound system. This model relies on two steps: 1) modelling of the effective magnetic susceptibility distribution around and within the TAG active mound using minimum-structure inverse modelling; 2) modelling the discrete contact boundaries between the deposit and surrounding basalt host rock using magnetic and gravity SGI. Our modelling has developed, to the best of our knowledge, the first 3D model of the TAG mound derived from geophysical data, an improved sulfide tonnage estimate evaluation for the deposit, and a better understanding of the deposit-scale hydrothermal fluid circulation.

2 Methods

Two modelling methods were used in this study, the minimum-structure inverse modelling method and the surface geometry inversion method. Both solve for the form of a spatial distribution of a physical property in the crust but do so in two fundamentally different ways.

2.1 Minimum-structure Inverse Modelling

The minimum-structure inversion method is arguably the most common inverse modelling method used in geophysical studies (Farquharson & Lelièvre, 2017). The method solves for a smooth distribution of the target physical property in the subsurface, generating a blurred subsurface model. A cell-based mesh is used during minimum-structure inversions, which discretizes the subsurface into several fixed voxels that each contain a homogeneous physical property value. In our minimum-structure magnetic modelling we use a tetrahedral discretization for all the inversions' meshes, as these unstructured meshes allow for very accurate representation of variable bathymetry on the surface of the mesh as well as being able to efficiently incorporate zones of variable mesh discretization (Lelièvre et al., 2012). To construct our meshes we use the program *Triangle* (Shewchuk, 1996) to develop a 2D Delaunay triangular surface to represent the bathymetric surface, and the program *Tetgen* (Si, 2015) to fill the 3D volume below the bathymetric surface with tetrahedra.

The minimum-structure inversion approach used here considers an objective function structured as,

$$\phi = \lambda \phi_d + \phi_m,$$

168 with an L2 norm data misfit

$$\phi_d = \frac{1}{N}\sum_{i=1}^{N}\frac{\left(d_{i,pred} - d_{i,obs}\right)^2}{\sigma_i^2} \qquad 2$$

and model measure ϕ_m. λ is the trade-off parameter between the data and model measure (Constable et al., 1987). The predicted data, $d_{i,pred}$, are calculated using Okabe (1979)'s algorithm, the observed data, $d_{i,obs}$, are the measured magnetic data with noise σ_i. The model measure only contains a smoothing term, as no smallness measure or reference model was used in the inverse modelling,

$$\phi_m = v_f^T W_s \left(D_f m \right)^2. \qquad 3$$

In Eq. 3 W_s is the weighting matrix, v_f the array of integration cell volumes, and D_f is the general difference matrix applied to the array of model parameters *m* (Lelièvre & Farquharson, 2013). In Eq. 3 the L2 norm is used on the model misfit (Constable et al., 1987), as well as a variation of Li & Oldenburg (2000) sensitivity weighting, to preferentially weight cells with low sensitivities, whose array is composed of elements

$$w_j = \left(\sum_{i=1}^{N} \left| \frac{G_{ij}}{v_j} \right|^2 \right)^{\frac{1}{2}}, \qquad 4$$

for the j^{th} cell in the mesh with N cells, whose volume is v_j. G denotes the inverse problem's sensitivity matrix, with elements G_{ij}.

2.2 Surface Geometry Inverse Modelling

The second inversion method used in this study is the SGI method of Galley et al., (2020b). Rather than solving for the physical properties in several cells, the SGI method holds the physical property values in a number of geometry bodies constant and alters the shape of the body until the predicted data sufficiently fit the observed geophysical data. Each of these anomalous bodies are parameterized by a surface tessellation of triangular facets, defining the discrete contact between differing geologic units. As such, the inversion method is parameterized by the 3D Cartesian coordinates of each vertex that defines the wireframe surface mesh. This parameterization often leaves the inverse problem over-determined, reducing the non-uniqueness of the problem compared to the under-determined minimum-structure method. Okabe (1979)'s forward algorithm was also used by this inversion program.

The topology of the SGI's wireframe surface mesh is not able to vary throughout the inversion, and as such its initial design holds some weight on how close of a data fit will be possible. To construct the wireframe surface meshes the program *FacetModeller* was used (Lelièvre et al., 2018), which allowed the user to place the defining vertices in 3D space and govern their connectivity through manual placement of the surface's triangular facets. As such, it is simple to incorporate any prior geologic information in the surface mesh, such as location of lithological contacts derived from borehole samples.

A GA was used to minimize the inversion's objective function, which is simply the data misfit, as the method's spatial parameterization has the possibility to add local minima to the solution space. After a best fit model is found from the GA a MCMC sampling is used to derive a model uncertainty and a mean inversion model.

An assumption that has been made in the developed SGI method's design is that the physical properties of each rock unit in the model remained fixed during the inversion. It is trivial to allow those physical properties to change as well as the surface geometry parameters (control node coordinates) by adding the physical properties of each homogeneous model region to the model

parameter vector. Instead, a suite of inversion models was produced with different physical property values, and these models were accessed relative to the drilling information to determine the best model.

211 # 3 Data

212 ## 3.1 Bathymetric Data

213 The bathymetric data were collected during the 2016 R/V Meteor M127 cruise using GEOMAR
214 AUV *Abyss,* equipped with a RESON Seabat 7125 multibeam echosounder. The echosounder
215 used a frequency of 200 kHz. The surveys were flown at a speed of 3 knots and line spacing of
216 80-100 m, resulting in a 2 m resolution bathymetric data set (Petersen and Shipboard Scientific
217 Party, 2016). The bathymetric data was merged with MB Systems based on the location of
218 prominent seafloor features, including the re-entry cone placed on the TAG mound during the
219 1994 ODP drilling that was visible in the high-resolution data. Erroneous soundings were
220 removed using QPS Qimera. From the original dataset a 3 by 3 km^2 region centered on the TAG
221 active mound was used in this study (Fig. 1a).

222 ## 3.2 Magnetic Data

223 During the M127 cruise, *Abyss* was equipped with an Applied Physics System APS 1540 Digital
224 3-Axis Miniature Fluxgate Magnetometer, which collected measurements at a 10 Hz sampling
225 rate. The magnetic data set was cropped to only include measurements within the 1.2x1.2 km^2
226 region centered on the TAG active mound (Fig. 2a). The magnetic dataset was processed to
227 remove the induced and permanent magnetization effects from the AUV by conducting a figure-
228 eight calibration dive with the AUV/magnetometer and using those data to solve for the AUV's
229 magnetic properties with a least-squares method (Honsho et al., 2013). The magnetic data were
230 also low-pass filtered with a 0.25 Hz cut-off to remove very short wavelength features associated
231 with noise and the effects of the AUV propeller. The dataset was then down-sampled to a point
232 every 50 m along the survey lines to reduce the computational expense of the inverse modelling,
233 without reduction in the quality of the constructed models. The 50 m down-sampling was done
234 while not producing any anti-aliasing artifacts.

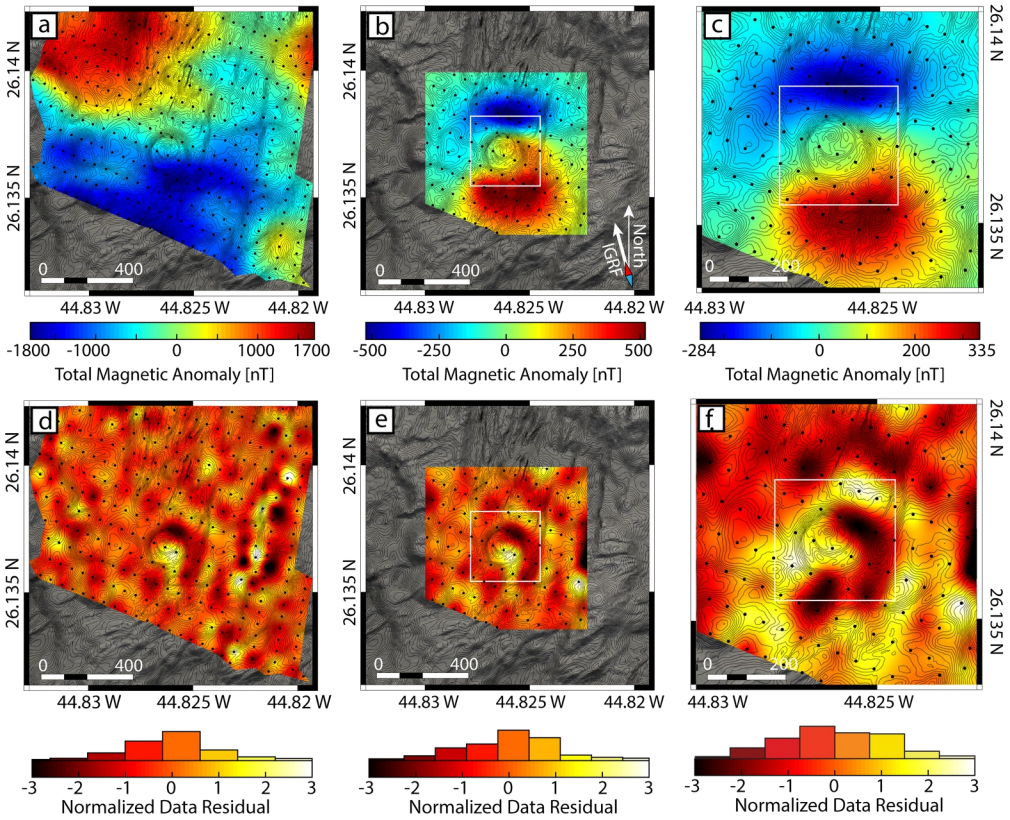

Figure 2. Processed data used in the magnetic inverse modelling. **a)** The total magnetic anomaly data measured during the RV Meteor M127 cruise, used in the regional minimum-structure inverse modelling; **b)** the regional-removed magnetic anomaly data used in the deposit-scale minimum-structure inverse modelling; **c** the regional-removed and filtered magnetic anomaly data used in the SGI; and **d-f)** are the respective normalized data residuals form the inversions of the data in **a-c**. In **b, c, e,** and **f** the white outline represents the extent of the deposit-scale mesh. In all images the locations of the observation points are shown as black dots and 5 m bathymetric contour lines are shown in black.

The magnetic data's noise is an unknown in this study. The magnetometer has very low system noise (quantified at 0.5 nT), but the uncertainty in the observation points' lateral positions creates a larger, secondary noise. In comparison, the vertical position of the AUV, determined from altimeter and depth readings collected while surveying, is more precise. The AUV's lateral position is tracked from an initial calibrated position using an inertial navigation system. Ideally, this would be able to accurately locate the position of the AUV throughout its surveying, but any seafloor currents will gradually shift it away from its inferred position. An 8% relative noise was assigned to the data, derived by adjusting how closely the study's minimum-structure inversion models could fit the data without producing artifacts. This noise would be equivalent to a 6-8 m uncertainty in the AUV's lateral position (Fig. S1).

3.3 Gravity Data

The dataset from the gravity survey collected over the TAG active mound was composed of 11 stations roughly aligned along a North-South line crossing the mound (Fig. 3a, b), collected during the 1994 R/V Yokosuka MODE'94 cruise. The measurements were collected manually from the Shinkai 6500 submersible on the seafloor with a Scintrex CG-3 autograv gravimeter (Evans, 1996). The data were first levelled using the northern most station as a reference point, then processed to develop the free-water anomaly,

$$g_F = \left(\gamma_a - 4\pi\rho_W G\right) D$$

5

¿ $0.222\,D$

where γ_a = 0.309 mGal/m is the free-air gradient, ρ_W = 1.02 g/cm^3 was used as the density of seawater, G is the gravitational constant, and D is the array of station elevation measurements relative to the reference station (Ishihara et al., 2018). The forward signal of a background model built with 2 m resolution bathymetric data of the seafloor about the mound, with density 2.4 g/cm^3 (Evans, 1996), was then removed to produce the Bouguer anomaly data. The 2 m resolution bathymetric data did not extend sufficiently far away from the observation points, so the linear trend left in the Bouguer anomaly data was calculated with a least-squares method and removed. The gravity data's noise was derived from the system noise of the gravimeter, as well as the compounding uncertainties associated with the data processing.

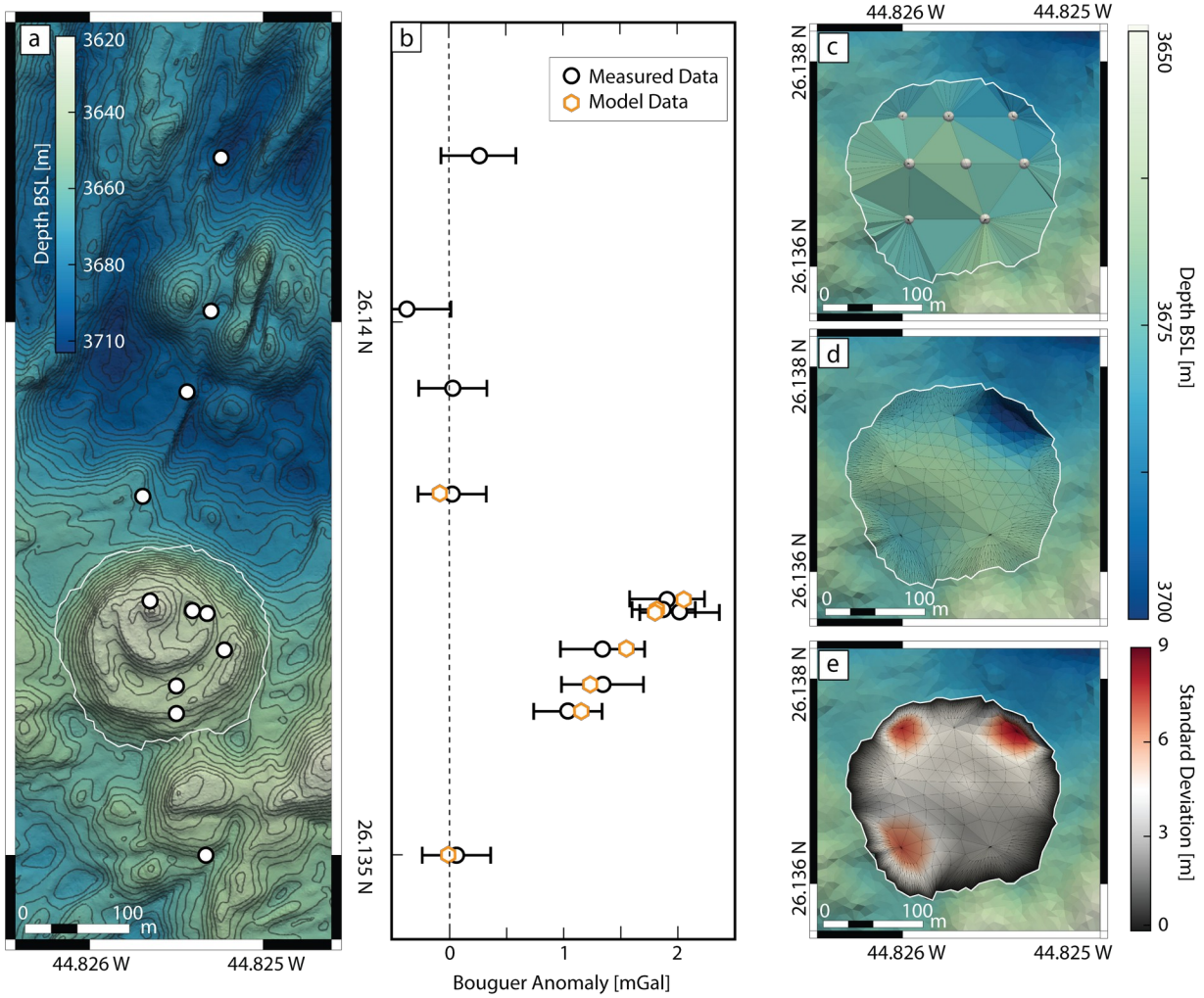

Figure 3. The gravity data collected over the TAG active mound as well as its SGI model. **a)** The locations of the gravity measurement stations are shown on the bathymetric map; **b)** a plot displaying the measured Bouguer anomaly data (black circles) compared to the data resulting from the SGI (orange hexagons); **c)** the initial model for the massive sulfide layer shown relative to the surrounding bathymetry; **d)** the SGI result relative to the surrounding bathymetry; and **e)** the SGI model colored based on the standard deviation of the vertical position of the surface model. The black contour lines in **a** mark 5 m depth intervals and the error bars in **b** signify the magnitude of the data's standard deviation.

4 Results

4.1 Magnetic Inverse Modelling

Two minimum-structure inversion models were constructed to produce first-pass three-dimensional magnetic susceptibility distributions that fit the observed data (Fig. 2a). Firstly, a regional minimum-structure model was produced (Fig. 4a), from which we could determine the volume of seafloor that fully encompasses the magnetic low representing the hydrothermal alteration associated with the deposit. Both magnetic inversion methods used in this study assume that the induced magnetic fields in the subsurface are parallel to the geomagnetic reference field, allowing the method to solve for the scalar effective magnetic susceptibility. To rule out the possible presence of remanent magnetization that might perturb the magnetization vectors in the crust away from the Earth's inducing field a total magnetization vector inversion (TMVI) was performed to access the variance in the inclination and declination of the magnetization vectors in the constructed model (Fig. S3; Lelièvre & Oldenburg, 2009). The result of this showed that there was little to no remanence oblique to the Earth's inducing field, allowing scalar magnetic susceptibility models to sufficiently reconstruct the crust's magnetic properties around the TAG mound. The larger scale, scalar magnetic inversion was solely used to determine the minimum volume of altered oceanic crust around the TAG mound, so that more focused inversion models could be constructed and studied.

To perform small-scale modelling of the deposit, a regional data removal was used to isolate a 300 by 300 by 300 m^3 volume enclosing the mound (Li & Oldenburg, 1998). The regionally-removed dataset was produced by creating a second regional inversion model that overfitted the magnetic data assuming a 0.3% noise. Over-fitting the data during the regional-removal process is key to ensuring that the remaining magnetic signal comes solely from the isolated volume. After isolating the volume of seafloor directly around the TAG active mound, the forward signal from the remainder of the model could be calculated and subtracted from the observed magnetic data to isolate the magnetic signature of the deposit (Fig. 2b; Li & Oldenburg, 1998). With the derived regional-removed data, a second inversion model could be produced with a much greater cell compactness (608,134 cells within a 300 by 300 by 330 m^3 volume, versus 443,749 cells within a 3 by 3 by 1.8 km^3 volume) and higher bathymetric surface resolution (an average triangular facet area of 2.7 m^2 versus 50 m^2), creating a more accurate minimum-structure inversion model of the TAG active mound (Fig. 4b). Comparing the magnetic features between the regional and deposit-scale inversion models affirms that the regional-removal did not subtract any data features that correspond to magnetic features in the isolated volume (Fig. 4). Both minimum-structure inversions used a positivity constraint on their effective magnetic susceptibility. The regional inversion took 25 iterations and 4.1 hours to complete, and the deposit-scale inversion took 24 iterations and 45 minutes. Each inversion was run in parallel on 48 threads on a 2.20 GHz Intel Xeon E5-2650 Processor.

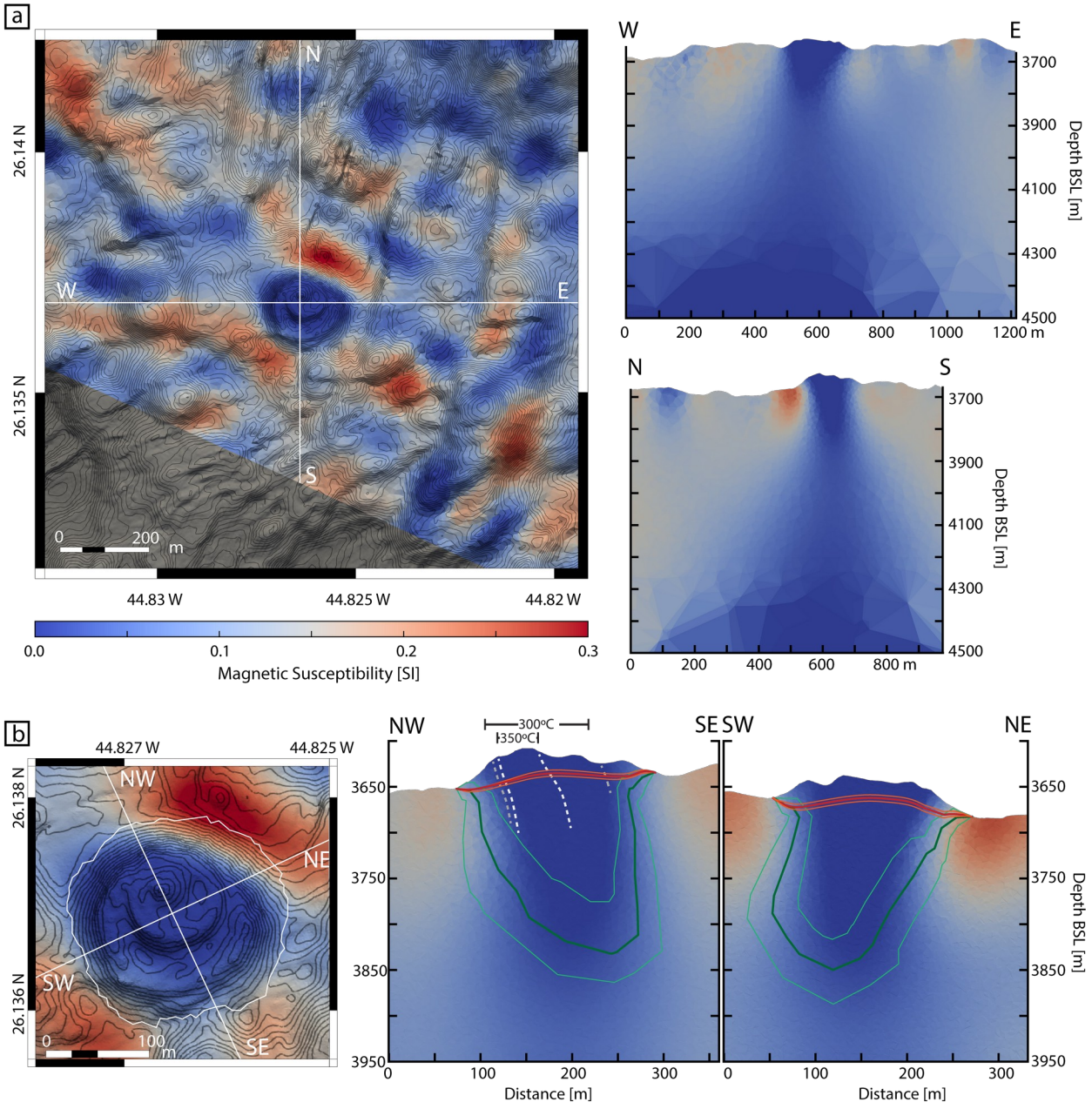

318

Figure 4. The minimum-structure inversion results from the regional and deposit-scale models. **a)** The regional model shown in plan view and West-East and North-South cross sections. **b)** The deposit scale minimum-structure model. The mean surface-intersect for the chloritized basalt SGI is shown as a dark green line, and the base of the massive sulfide SGI layer in red. The one standard deviation shifted models are shown as a light green line for the chloritized basalt model, and orange for the massive sulfide model. Bathymetric contour lines (5 m interval) are shown in black. In the deposit-scale cross sections isotherms are overlain onto the bathymetry to compare with the geometry of the magnetic low anomaly (Grant et al., 2018).

Next, we applied an additional processing procedure to further refine the magnetic data near the TAG active mound in preparation for the more targeted SGI modelling. Ideally, when constructing surface models of the subsurface one would want a homogeneous background with the single anomalous body contained within. However, the crust directly adjacent to the TAG active mound is inhomogeneous, containing zones of anomalously high magnetic susceptibility near the seafloor likely indicating areas of younger extrusive rocks (Fig. 4b). To remove the components of the magnetic data that correspond to the anomalously high regions, a five step workflow was developed (Fig. 5): 1) invert the data derived from the regional removal; 2) isolate the cells that contain magnetic susceptibilities above the observed background value in the regional inversion model (in this case 0.08 SI; Fig. 4b), subtract the background value from the magnetic susceptibilities in the isolated cells to get anomalous susceptibilities relative to the background (0.08 SI); 3) calculate the forward signal from the isolated cells derived from step 2; 4) subtract the isolated cells' forward signal from the regional-removed data; and 5) invert the resulting data set to create a magnetic susceptibility model effectively free of anomalously high magnetic susceptibility regions.

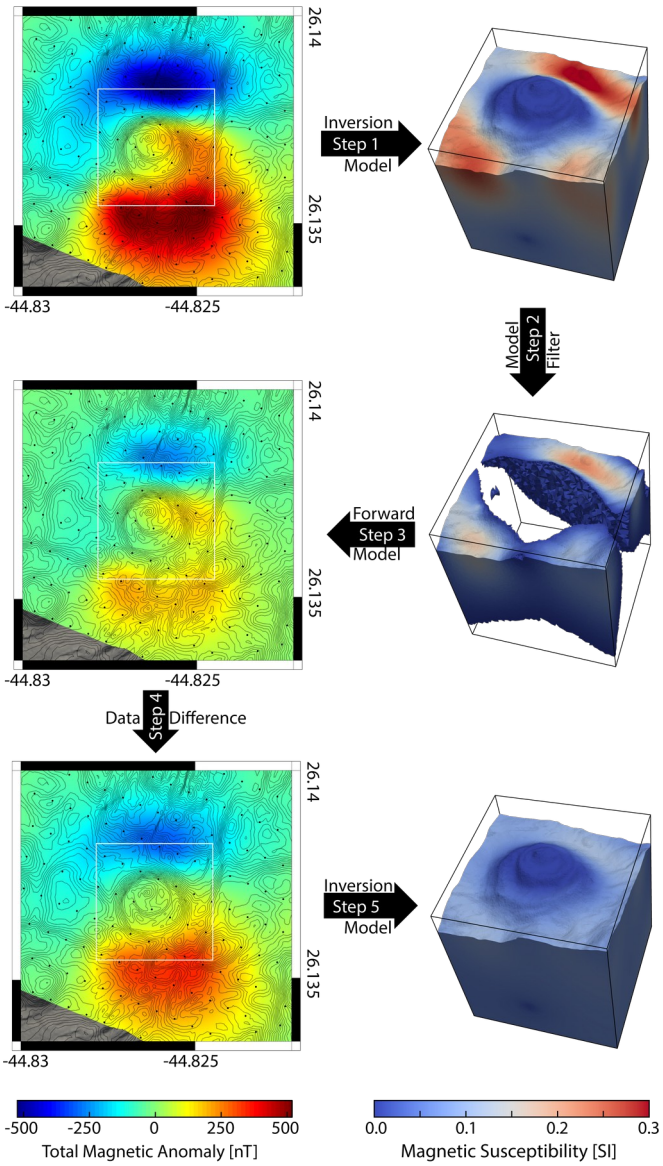

Figure 5. The workflow to deprive the magnetic data from undesirable anomalously high magnetically susceptible regions of a voxel inversion model.

The background value of 0.08 SI was chosen from the distribution of magnetic susceptibilities in the regional-removed model. As seen in Figure 6, there are 2 major peaks in the histograms, one about 0.0 SI representing the anomalously low magnetic susceptibility of the TAG active mound, and the second at 0.08 SI representing the background. The curve representing the model's background magnetic susceptibility in the regional-removed model is wider compared to the filtered model. After further processing the data by removing the signal components related to the high magnetic susceptibility region (Fig. 5), the filtered model distribution develops a more prominent mean at 0.07-0.075 SI bin (Fig. 6). Fitting a normal distribution to the background susceptibility values in the filtered model results in an approximate distribution with mean 0.07 SI and 0.01 SI standard deviation.

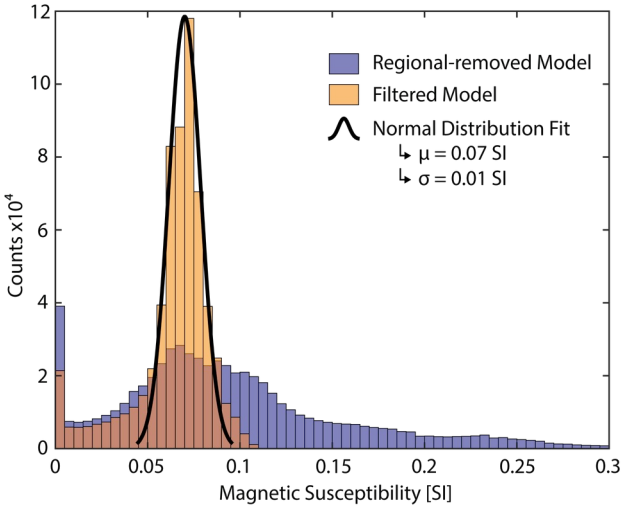

Figure 6. Two histograms representing the distribution of magnetic susceptibility values in the cells of the region-removed and 0.08 SI filtered models.

An SGI can now be performed on the resulting filtered data (Fig. 2c) to model the TAG active mound as an anomalous low inside an approximately homogeneous background. The first step in our SGI is to design an initial model for the inversion. Spatial bounds are then applied to the model vertices to develop an initialization volume. The initialization volume is defined as the volume of space that the solution model is assumed to exist in and acts as the search volume during the inversion process. For the TAG active mound, the drillcore provide enough information to develop an initial model.

The initial model for the chloritized basalt (Fig. 7a, b) was defined as the inferred inner surface of this alteration type (see Fig. 1b for the drilling information), acting as a minimum volume that the SGI would then expand. The surface model was composed of 14 vertices, each of which could move in all three dimensions, resulting in 42 inversion parameters for the SGI. We held the model's physical properties constant throughout the inversion, using a value of 10^{-5} SI for the TAG active mound (Zhao et al., 1998), and a value of 0.08 SI for the background, as derived from the voxel inverse modelling. To bound the vertices in 3D, relative to their initial position (see Fig. 7a, b), constraints were assigned: +/- 30 m for the upper seven vertices in the horizontal (East-West and North-South) plane, and vertical constraint of +0 m/-20 m; +/- 100 m horizontally for the lower seven vertices, and +20 m/-300 m vertically.

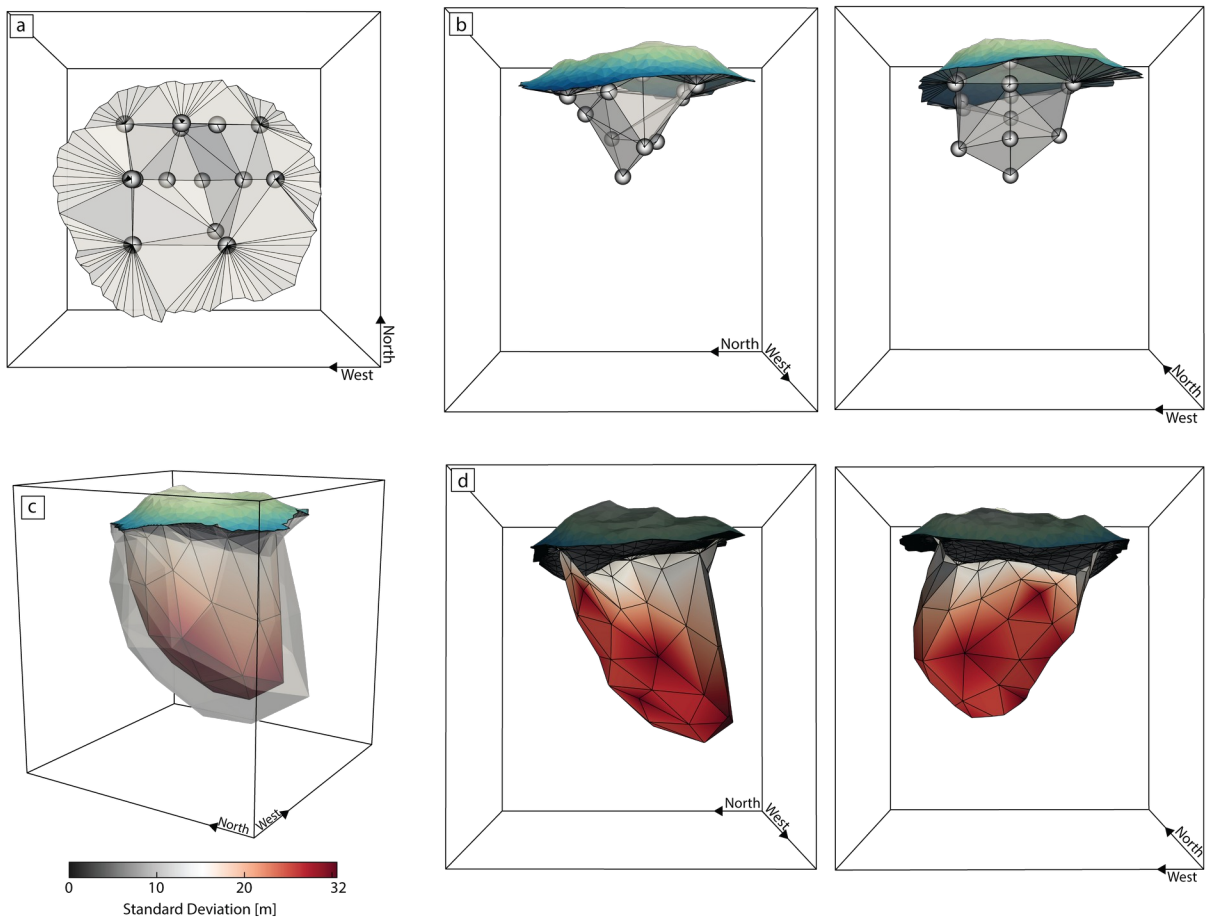

379 **Figure 7.** The initial model **a, b** and inversion result **c, d** for the magnetic SGI. **a)** The plan view
380 of the initial magnetic model with the bathymetry surface of TAG removed, and **b)** the same
381 model including the bathymetric surface side on. The vertices of the initial model are grey
382 spheres, and the top of the TAG active mound is colored based on its bathymetry. **c)** The TAG
383 active mound's sub-seafloor hydrothermal alteration SGI model result, with the mean model
384 colored based off its vertices' standard deviations. The translucent grey surface is the mean
385 model expanded by one standard deviation. **d**) Two half-slices of the magnetic and gravity SGI
386 models, colored by the surfaces' vertices' standard deviations.

387

388 As the physical properties in the SGI model are constant throughout the modelling, some
389 uncertainty assessment is required to justify the choice of the anomalous and background
390 susceptibilities. The assessment was performed by creating a suite of SGI models with varying
391 magnetic susceptibility values, comparing the different models to the active mound's drillcore,
392 then choosing the most geologically accurate model. The range of background magnetic
393 susceptibilities were chosen from the fitted normal distribution of Fig. 6, which had a mean of
394 0.07 SI and a standard deviation of 0.01 SI, created a range of [0.06, 0.08] SI. SGI models
395 created with background susceptibilities of less and or equal to 0.075 SI produced a chloritized
396 basalt model that was too small and did not agree with the bounds on the alteration units as
397 defined from the drillcore. Models inverted with background values of 0.07, 0.075, and 0.08 SI
398 (Fig. 8a) demonstrating the change in model geometry that results from using different magnetic
399 susceptibility values. Within the 0.07+/-0.01 SI range the background value of 0.08 SI produced
400 the best model, agreeing most with the drillcore.

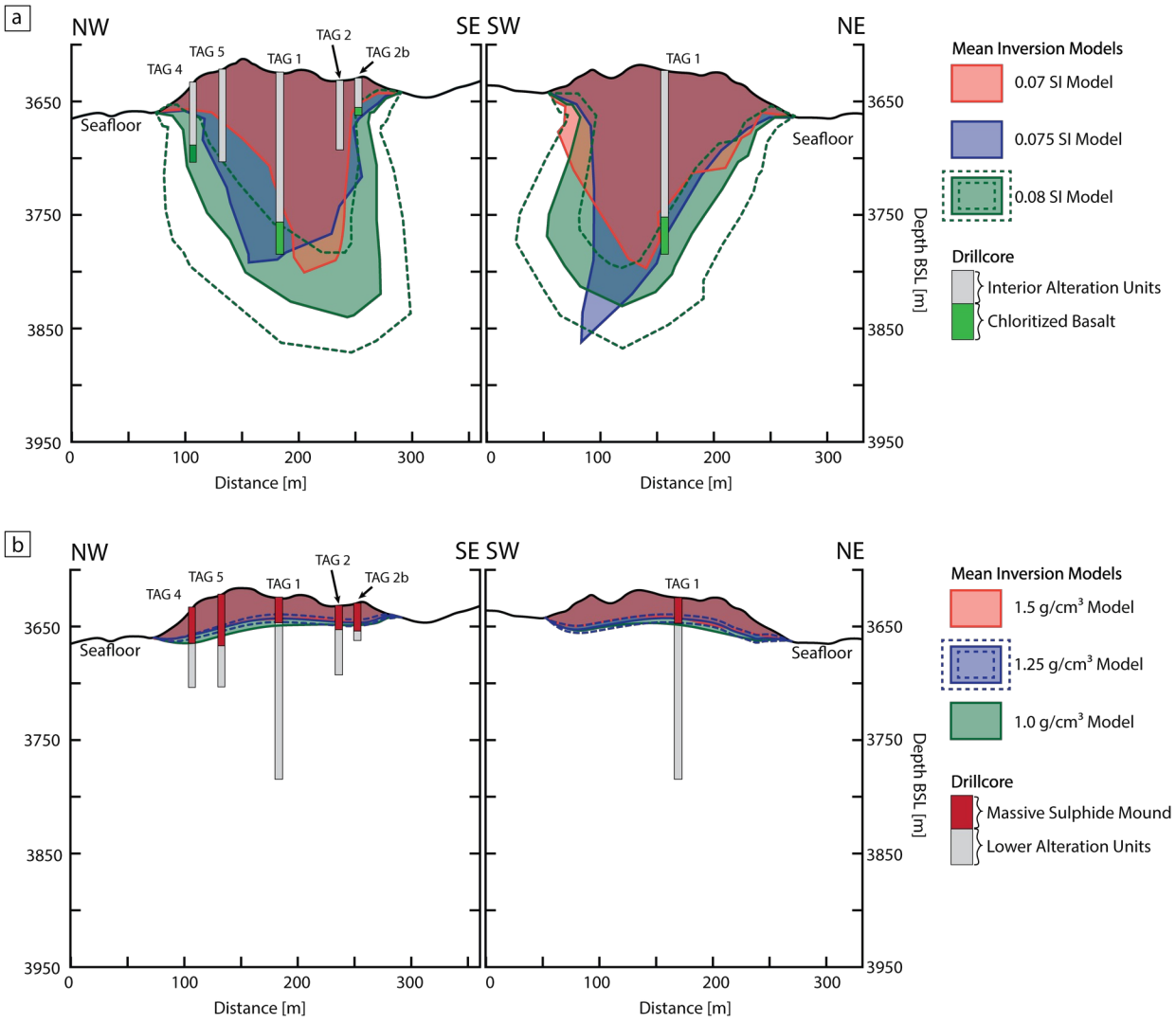

Figure 8. A comparison on the geometry of **a)** the magnetic SGI model inverted with three different background magnetic susceptibility values: 0.07, 0.075, and 0.08 SI, and **b)** the gravity model with anomalous mound densities of 1.0, 1.25, and 1.5 g/cm^3. The anomalous density being the contrast between the massive sulfide mound's density and the background basalt's density. Each of the 3D models are shown as two cross-sections, the left cross-section running parallel to the drillcores, and the right-hand cross-section perpendicular to it, following the same orientations as in Fig. 4b. In **a** and **b** the dotted lines represent a one standard deviation uncertainty on the position of the model's vertices.

The SGI for the chloritized basalt model took 90 seconds to complete the GA optimization, and 5.5 hours to complete the MCMC sampling (see Fig. S2 for the convergence curves). Both programs were run on 48 threads on a 2.20 GHz Intel Xeon E5-2650 Processor, with the GA running in parallel and the MCMC in serial. The result of the magnetic SGI is shown in Figure 4b compared to the magnetic voxel inversion model, and again in Fig. 7c, d.

4.2 Gravity Inverse Modelling

As the gravity data only consisted of 11 stations, all roughly along a north-south line, a minimum-structure inversion of the data would be poorly constrained and produce an ambiguous subsurface model. Therefore, only SGI models were created from the gravity data. Of the eleven stations, only the eight closest to the TAG mound were used to develop the SGI model as the other three had low signal sensitivity to the density of the TAG mound.

The initial model for the base of the massive sulfide layer (Fig. 3c) was derived from the available drillcore data. The vertices for the gravity SGI were constrained with +10 m/-50 m bounds relative to the starting model solely in the vertical direction, as the model for the massive sulfide was already well constrained from the drilling. Density values of 3.65 g/cm^3 and 2.4 g/cm^3 were used for the massive sulfide lens and underlying crust, respectively (Evans, 1996). As discussed in Graber et al. (2020), a range of densities have been used to represent the TAG active mound's massive sulfide, from 3.5 g/cm^3 to 3.8 g/cm^3. Therefore, a reasonable uncertainty on our choice of 3.65 g/cm^3 would be +/- 0.15 g/cm^3. The 2.4 g/cm^3 density for the background basalt was chosen as it provided the best fit to the data while performing the Bouguer anomaly regional signal removal. Densities of 2.3 g/cm^3 and 2.5 g/cm^3 provided adequate fits as well, which would result in an effective background uncertainty of +/- 0.1 g/cm^3. As the SGI forward solver calculated the gravitational signal of each facet in the surface model based off the difference in densities across the facet, the uncertainty of the difference in density between the massive sulfide mound and background basalt will be the sum of the individual uncertainties, i.e. +/- 0.25 g/cm^3.

Therefore, the eight vertices used to define the massive sulfide layer model resulted in eight inversion variables. The subsequent SGI took 40 seconds to complete the GA, and 45 minutes to complete the MCMC sampling.

439 The gravity SGI resulted in a model of the lower surface of the massive sulfide mound,
440 separating the lens from the altered seafloor crust. The volume of rock contained between the
441 gravity model and the TAG active mound's bathymetric surface then approximates the volume of
442 massive sulfide contained in the lens. The massive sulfide lens model has an approximate
443 volume of 594, 000 +/- 120,000 m^3, which would indicate 2.17 +/-0.44 Mt of material assuming
444 the 3.65 g/cm^3 density used during the modelling, as used in Evans (1996). Figure 8b shows the
445 SGI results using three density contrasts within the range of +/- 0.25 g/cm^3 about the chosen 3.65
446 - 2.4 = 1.25 g/cm^3 contrast. This comparison indicates the uncertainty on the geometry of the
447 massive sulfide lens resulting from an uncertainty in the chosen density values.

448

449 **5 Discussion**

450 The two SGI models produced in this study provide new information on two important aspects of
451 the TAG active mound: 1) the inversion of the gravity data provides a 3D model for the thickness
452 of the massive sulfide layer of the deposit; and 2) the inversion of the magnetic data creates an
453 enclosing surface representing the outer extent of the chlorite-rich hydrothermal alteration of
454 basalt beneath the deposit. The outer extent of the chloritized basalt will therefore indicate the
455 depth and location of mixing between hydrothermal fluid and seawater at temperatures greater
456 than 200°C. An updated geologic interpretation, in 3D, was made by combining the SGI surfaces
457 with inferred interface information from the drillcore (Fig. 9).

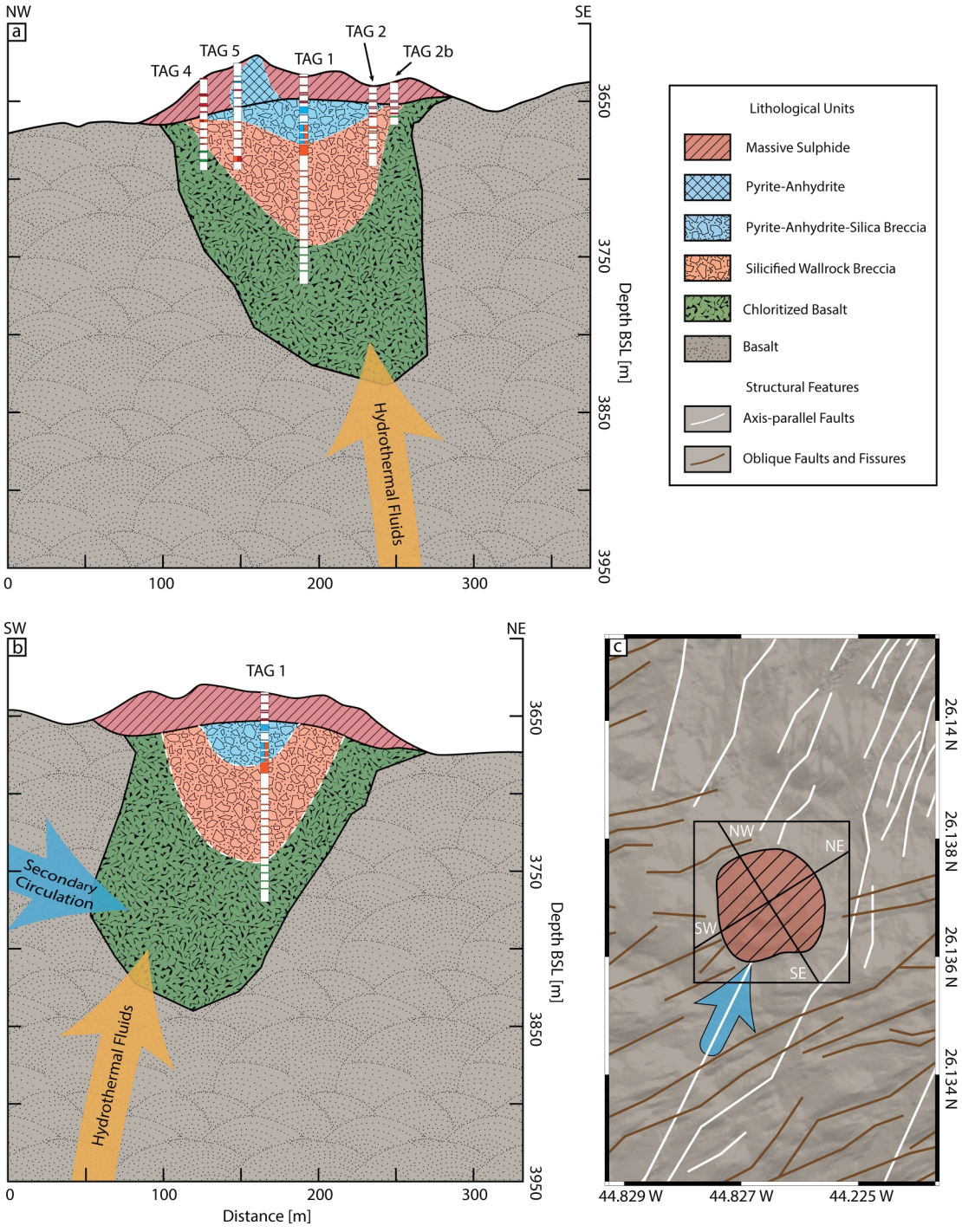

458

459 **Figure 9.** Two geological cross sections of the TAG active mound derived through gravity and
460 magnetic geophysical inverse modelling and drillcore information. The cross-section **a** is
461 oriented parallel to the drillholes and **b** orthogonal to them. Dotted white lines indicate inferred
462 surfaces derived from the rock samples retrieved through drilling, and the solid black lines
463 represent the surfaces created through SGI modelling. In both cross-sections the white space
464 along the drillholes represents locations with zero recovery. **c** shows a plan view of the deposit
465 with the interpreted vector for secondary circulation of seawater.

466

467 Although the ODP Leg 158 drillholes were used to design the initial mode for the SGIs, their
468 information did not bias results or influence the inversions once they started. The initial models
469 provided a geometry and topology that should be somewhat close to the actual form of the active
470 mound's rock units, but once the inversions began the models' vertices moved within their
471 positional constraints without influence from the initial model. The drillcore information was
472 used to decide what background magnetic susceptibility to use, as multiple susceptibility values
473 were used to construct a suite of SGI models but only the 0.08 SI background model was both
474 statistically appropriate as a background value as well as agreed with the drillcore. There were no
475 chloritized basalt-basalt intersections in the drillcore to compare the magnetic SGI to, but the
476 gravity SGI surface correlates closely with the bottom most collected massive sulfide samples
477 (Fig. 9).

The chloritized basalt model, which extends to ~150 m below the seafloor, indicates infiltration of local seawater (i.e. secondary circulation; Fig. 9) that approaches the base of the mound from the South-West in line with the axis-parallel faulting passing through the mound (Fig. 1a). Pontbriand & Sohn (2014) determined a similar geometry for the secondary circulation through mapping the location of micro seismic events attributed to the precipitation of anhydrite at the locations of local seawater infiltration near the TAG mound. Their results showed a zone of high seismic event density to the immediate South-West of the mound, from the near surface to a depth of 125 m below the seafloor. This suggests that although the rising hydrothermal fluids are assumed to be approaching from the north-west on the regional scale (normal to the spreading axis; Szitkar et al., 2015), the locally infiltrating seawater and near surface component of the upflow zone approaches the active mound along axis parallel faulting. The axis parallel faulting is present at both the North and South of the TAG mound, but the southern faults are heavily cross-cut by axis-oblique faults and fissures (Fig. 1a).

Comparing the geometry of the modelled chloritized basalt unit to ancient VMS systems, primarily Cyprus-type deposits that have relatively undeformed alteration zones, the chlorite alteration units can have a range of thicknesses. The thicknesses of the units at the Mathiati deposit are 10-50 m, and 100-200 m thick at the Skouriotissa deposit (Hannington et al., 1998). These thicknesses are proportional to the size of the deposits, as a larger ore lens relates to a larger stockwork system, but they do compare to the 10-75 m thick modelled chloritized basalt unit for the TAG active mound.

Using the massive sulfide lens SGI model, the volume of rock contained between it and the overlying bathymetric surface was calculated to be 595,000 m^3 +/- 20%. The derived tonnage of 2.17 +/-0.44 Mt of rock is in agreement with Graber et al., (2020)'s 2.27 Mt approximation, which was measured by placing an interpolated surface through the TAG mound to separate the unit of massive sulfide from the altered crust (Jamieson et al., 2014) and assuming a 3.5 g/cm^3 density. If 3.65 g/cm^3 was assumed for the density in Graber et al., (2020)'s it would have resulted in 2.37 Mt, still in agreement with 2.17 +/-0.44 Mt. As seen in Figure 3d, the base of the massive sulfide lens matches closely with the form of the surrounding bathymetric surface, most notably observed by the raised region in the center of the mound aligning with the raised pillow mound terrain noted in Graber et al. (2020). The other study that approximated the massive sulfide tonnage in the TAG active mound was Hannington et al. (1998), that used a blocky model of cylindrical units. Their calculated tonnage was 2.7 Mt for the massive sulfide lens, higher than the value derived from this study's model and that of Graber et al. (2020). This is most likely caused by the relatively large size of the units in the blocky model adding extra volume as the five cylinders at the top of the model could not accurately fit the active mound's topography. Additionally, Hannington et al. (1998) used a 3.8 g/cm^3 density in their calculations; if 3.65 g/cm^3 was used as in this study their tonnage would be 2.6 Mt.

In analysis of the geometry of the massive sulfide mound's inversion model, the downward concavity of the mound's base implies that the replacement alteration of the seafloor below the mound did not significantly increase its density. The alteration below the mound is composed of basalt brecciated with veins of silicate, sulfide, and sulfate minerals. The density for these lower alteration units and the background basalt used in this study was 2.4 +/- 0.1g/cm^3. Since the density of the replacement alteration units appears similar to the unaltered basalt, it would imply that there is not a significant amount of higher density massive sulfide present in that region. However, this would contradict the samples collected from ODP Leg 158 which recorded average of 34 % composition of pyrite in the pyrite-anhydrite-silica breccia and the silicified wallrock breccia units (Ludwig et al., 1998). A possible explanation for the density of altered seafloor is that the drillcore recovery efficiency, which was 12% in Leg 158 (Humphris & Tivey, 2000), is biased towards intervals that contain abundant higher density sulfide minerals. The higher density intervals would not crumble so easily during the drilling and would remain intact during retrieval. There might therefore be a lower amount of pyrite present in the seafloor below the massive sulfide lens than the Leg 158 drilling suggests. Of the samples recovered during the Leg 158 drilling, their mean percent composition was 34 % sulfide, 4.5 % anhydrite, 58 % quartz, and 3 % clay (Ludwig et al., 1998). Treating the composition of the recovered 12 % of the core as representative of 12 % of the stockwork zone, a geologic model of the remaining 88 % was constructed to determine its composition. The model is made up of percentages of pyrite (5 g/cm^3; Sharma, 1997), quartz (2.65 g/cm^3; Sharma, 1997), anhydrite/basalt (2.9 g/cm^3; Sharma, 1997) and pore fluid (0.9 g/cm^3; Bischoff & Pitzer, 1985), while constrained by the modeled bulk density of the stockwork zone (2.4 g/cm^3) and that the percentages of the minerals and porosity sum to 100 %,

$$2.4\,g/cm^3 = \%_{pyrite}\cdot(5\,g/cm^3)+\%_{quartz}\cdot(2.65\,g/cm^3)+\%_{basalt}\cdot(2.9\,g/cm^3)+\%_{porosity}\cdot(0.9\,g/cn \qquad 6$$

$$100\,\% = \%_{pyrite}+\%_{quartz}+\%_{basalt}+\%_{porosity}. \qquad 7$$

As seen in Fig. 10, the indicated upper bound of pyrite possible in the stockwork zone would be 30 % (at a porosity of 63 %), with the lower bound being the 4.1 % already observed in the drillcore. It is unlikely that the stockwork zone's alteration would greatly increase its porosity, with some studies indicating that the alteration instead decreases porosity with the precipitation of sulfides, sulfates, and silicates (Wilkens et al., 1991; Zhu et al., 2007). Therefore, the percent volume of pyrite in the stockwork zone might be better constrained by considering porosities equal to or less than the background basalt's 26 %. This would indicate that at most 7.9 % of the stockwork zone would be composed of pyrite, occurring when there is zero basalt or anhydrite remaining and the alteration zone is solely sulfides and silicates.

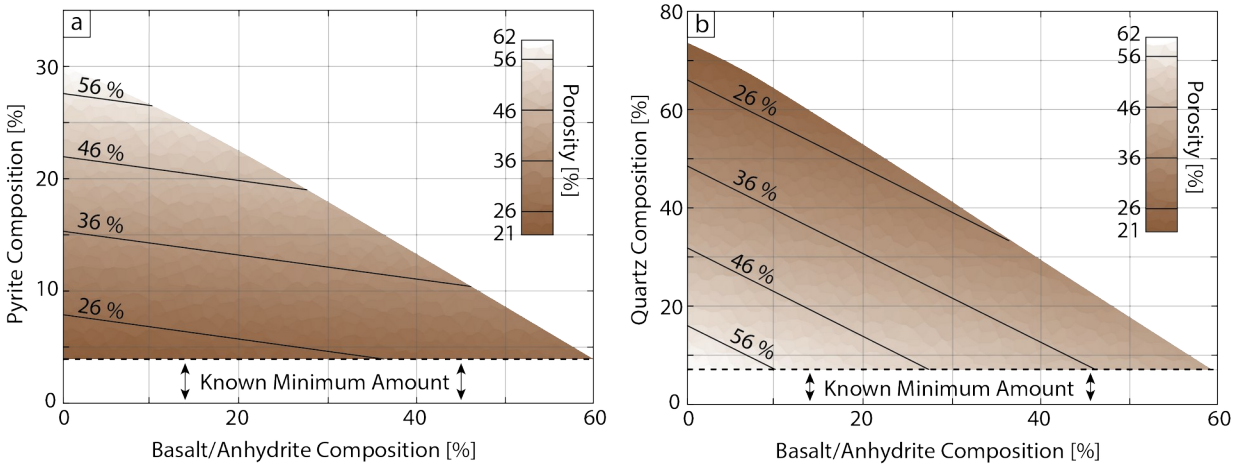

Figure 10. A geologic model of the percent composition of pyrite, quartz, basalt/anhydrite, and pore fluid that makes up the TAG active mound's stockwork zone. **a)** a plot showing the percent composition of pyrite versus the composition of basalt/anhydrite, with each black line representing a constant porosity, at intervals of 10 % from the background value of 26 %. **b)** the same style of plot for quartz versus basalt/anhydrite.

Our magnetic modelling assumed that all significant magnetization in the crust around the TAG active mound was parallel to the Earth's inducing field, although some previous studies have suggested that remanent magnetization oblique to the Earth's field might be present. Szitkar & Dyment (2015) found through magnetic forward modelling that the crustal magnetization under the TAG mound was rotated from the International Geomagnetic Reference Field's (IGRF) 42° inclination and -15° declination to a 10° inclination and 0° declination. This 53° rotation of the crust's magnetization about an axis parallel to the Mid-Ocean Ridge axis was inferred to be caused by the detachment fault tectonics in the region. To consider the presence of remanent magnetization oblique to the Earth's inducing field vector a TMVI model was created to study any significant deviations of the model's magnetization vectors (Fig. S3). The results indicated that the models showed a strong preference to have their magnetization in-line with the IGRF vector, with small groupings of cells containing oblique magnetizations, with respect to the IGRF, being associated with overfitting of the data. The effective magnetic susceptibility TMVI model contains less heterogeneities in the crust surrounding the TAG active mound, as given more degrees of freedom (i.e. effective magnetic susceptibility, inclination and declination, versus simply effective magnetic susceptibility as in the scalar magnetic inversion model) the TMVI program used near-surface variations from the IGRF direction to better fit the data rather than varying purely the effective magnetic susceptibility.

A limitation of the gravity and magnetic modelling of SMS deposits is the inability of these data to resolve the size and geometry of the silicified wallrock stockwork breccia zone below the massive sulfide lens. This zone may contain a significant portion of the deposit's precious and base metals and determining its volume would be of economic importance. Future work should combine the gravity and magnetic modelling with CSEM surveying (e.g. Gehrmann et al., 2019; Haroon et al., 2018) and seismic modelling (e.g. Murton et al., 2019) to also resolve the stockwork zone.

6 Conclusions

With the use of surface geometry inversion, sparse drilling and minimum-structure inversion results was further refined to develop a more comprehensive 3D wireframe geologic model of the TAG active mound. These wireframe models are composed of surfaces representing the discrete contacts between different rock units, which, in the case of the TAG active mound, was the interface between the massive sulfide lens and the underlying altered basalt, and the interface between the chloritized basalt and the unaltered/minimally altered background basalt. Our gravity inversion model presented a 2.17 +/- 0.44 Mt massive sulfide estimate for and anhydrite contained in the deposit's mound, and the magnetic inversion modelled the maximum depth where infiltrating seawater mixes with the rising hydrothermal fluids. The model is however limited in its inability to resolve the geometry of the deposit's silicified wallrock breccia zone, but through the future integration of other geophysical surveying methods this could be amended.

Acknowledgments

We would like to thank the captain, crew and scientific team from the 2016 R/V Meteor M127 and 1994 R/V Yokosuka MODE'94 cruises for all their work collecting the data modelled in this study. C.F. and C.G. are funded through an NSERC Discovery Grant and Memorial University's School of Graduate Studies Grant. The bathymetric and magnetic data is available from Petersen et al. (2019) (https://doi.pangaea.de/10.1594/PANGAEA.899415) and the gravity data will be available on Interdisciplinary Earth Data Allicance. The inversion software used to create the models for this study is property of Memorial University of Newfoundland and is available upon request from the authors.

Bibliography

Bischoff, J. L., & Pitzer, K. S. (1985). Phase relations and adiabats in boiling seafloor geothermal systems. *Earth and Planetary Science Letters*, *75*(4), 327–338. https://doi.org/10.1016/0012-821X(85)90177-3

Bouligand, C., Tivey, M. A., Finn, C. A., Morgan, L. A., Shanks, W. C. P., & Sohn, R. A. (2020). Geological and Thermal Control of the Hydrothermal System in Northern

608 Yellowstone Lake: Inferences From High-Resolution Magnetic Surveys. *Journal of*
609 *Geophysical Research: Solid Earth*, *125*(9). https://doi.org/10.1029/2020JB019743

610 Caratori Tontini, F., De Ronde, C. E. J., Yoerger, D., Kinsey, J., & Tivey, M. (2012). 3-D
611 focused inversion of near-seafloor magnetic data with application to the Brothers volcano
612 hydrothermal system, Southern Pacific Ocean, New Zealand. *Journal of Geophysical*
613 *Research: Solid Earth*, *117*(10), 1–12. https://doi.org/10.1029/2012JB009349

614 Constable, S. C., Parker, R. L., & Constable, C. G. (1987). Occam's inversion: A practical
615 algorithm for generating smooth models from electromagnetic sounding data. *Geophysics*,
616 *52*(3), 289–300.

617 Evans, R. L. (1996). A seafloor gravity profile across the TAG hydrothermal mound.
618 *Geophysical Research Letters*, *23*(23), 3447–3450. https://doi.org/10.1029/96GL00734

619 Farquharson, C. G., & Lelièvre, P. G. (2017). Modelling and Inversion for Mineral Exploration
620 Geophysics: A Review of Recent Progress, the Current State-of-the-Art, and Future
621 Directions. *Proceedings of Exploration 17: Sixth Decennial International Conference on*
622 *Mineral Exploration*, *17*, 51–74. http://www.dmec.ca/getattachment/7caa09d0-cfd7-4248-
623 ab1d-53b67ca65f24/Resources/Exploration-17/Modelling-and-Inversion-for-Mineral-
624 Exploration-Ge.aspx

625 Galley, A. G., & Koski, R. A. (1999). Setting and characteristics of ophiolite-hosted
626 volcanogenic massive sulphide deposits. *Reviews in Economic Geology*, *8*, 221–246.

627 Galley, A., Hannington, M. D., & Jonasson, I. (2007). Volcanogenic massive sulphide deposits.
628 Mineral deposits of Canada: A synthesis of major deposit-types, district metallogeny, the
629 evolution of geological provinces, and exploration methods: Geological Association of
630 Canada. *Mineral Deposits Division, Special Publication.*, *5*(6), 141–161.

631 Galley, C. G., Jamieson, J. W., Lelièvre, P. G., Farquharson, C. G., & Parianos, J. M. (2020).
632 Magnetic imaging of subseafloor hydrothermal fluid circulation pathways. *Science*
633 *Advances*, *6*(44), 1–11. https://doi.org/10.1126/sciadv.abc6844

634 Galley, C. G., Lelièvre, P. G., & Farquharson, C. G. (2020). Geophysical inversion for 3D

635 contact surface geometry. *Geophysics*, *85*(6), 1–76. https://doi.org/10.1190/geo2019-0614.1

636 Gehrmann, R. A. S., North, L. J., Graber, S., Szitkar, F., Petersen, S., Minshull, T. A., & Murton,
637 B. J. (2019). Marine Mineral Exploration With Controlled Source Electromagnetics at the
638 TAG Hydrothermal Field, 26°N Mid-Atlantic Ridge. *Geophysical Research Letters*, *46*(11),
639 5808–5816. https://doi.org/10.1029/2019GL082928

640 Graber, S., Petersen, S., Yeo, I., Szitkar, F., Klischies, M., Jamieson, J., Hannington, M.,
641 Rothenbeck, M., Wenzlaff, E., Augustin, N., & Stobbs, I. (2020). Structural Control,
642 Evolution, and Accumulation Rates of Massive Sulfides in the TAG Hydrothermal Field.
643 *Geochemistry, Geophysics, Geosystems*, *21*(9). https://doi.org/10.1029/2020GC009185

644 Grant, H. L. J., Hannington, M. D., Petersen, S., Frische, M., & Fuchs, S. H. (2018). Constraints
645 on the behavior of trace elements in the actively-forming TAG deposit, Mid-Atlantic Ridge,
646 based on LA-ICP-MS analyses of pyrite. *Chemical Geology*, *498*(July), 45–71.
647 https://doi.org/10.1016/j.chemgeo.2018.08.019

648 Hannington, M. D., Galley, A. G., Gerzig, P. M., & Petersen, S. (1998). Comparison of the TAG
649 mound and stockwork complex with Cyprus-type massive sulfide deposits. *Proceedings of*
650 *the Ocean Drilling Program: Scientific Results*, *158*, 389–415.
651 https://doi.org/10.2973/odp.proc.sr.158.217.1998

652 Hannington, M., Jamieson, J., Monecke, T., Petersen, S., & Beaulieu, S. (2011). The abundance
653 of seafloor massive sulfide deposits. *Geology*, *39*(12), 1155–1158.
654 https://doi.org/10.1130/G32468.1

655 Haroon, A., Hölz, S., Gehrmann, R. A. S., Attias, E., Jegen, M., Minshull, T. A., & Murton, B. J.
656 (2018). Marine dipole-dipole controlled source electromagnetic and coincident-loop
657 transient electromagnetic experiments to detect seafloor massive sulphides: Effects of three-
658 dimensional bathymetry. *Geophysical Journal International*, *215*(3), 2156–2171.
659 https://doi.org/10.1093/gji/ggy398

660 Honsho, C., Ura, T., & Kim, K. (2013). Deep-sea magnetic vector anomalies over the Hakurei
661 hydrothermal field and the Bayonnaise knoll caldera, Izu-Ogasawara arc, Japan. *Journal of*

662 *Geophysical Research: Solid Earth*, *118*(10), 5147–5164.
663 https://doi.org/10.1002/jgrb.50382

664 Honsho, C., Ura, T., & Tamaki, K. (2012). The inversion of deep-sea magnetic anomalies using
665 Akaike's Bayesian information criterion. *Journal of Geophysical Research: Solid Earth*,
666 *117*(1), 1–12. https://doi.org/10.1029/2011JB008611

667 Humphris, S. E., Alt, J. C., Teagle, D. A. H., & Honnorez, J. J. (1998). Geochemical changes
668 during hydrothermal alteration of basement in the stockwork beneath the active TAG
669 hydrothermal mound. *Proceedings of the Ocean Drilling Program: Scientific Results*, *158*,
670 255–276. https://doi.org/10.2973/odp.proc.sr.158.220.1998

671 Humphris, S. E., & Tivey, M. K. (2000). A synthesis of geological and geochemical
672 investigations of the TAG hydrothermal field: Insights into fluid-flow and mixing processes
673 in a hydrothermal system. *Special Papers-Geological Society of America*, *349*, 213–235.

674 Humphris, Susan E., Herzig, P. M., Miller, D. J., Alt, J. C., Becker, K., Brown, D., Brügmann,
675 G., Chiba, H., Fouquet, Y., Gemmell, J. B., Guerin, G., Hannington, M. D., Holm, N. G.,
676 Honnorez, J. J., Iturrino, G. J., Knott, R., Ludwig, R., Nakamura, K., Petersen, S., … Zhao,
677 X. (1995). The internal structure of an active sea-floor massive sulphide deposit. *Nature*,
678 *377*(6551), 713–716. https://doi.org/10.1038/377713a0

679 Ishihara, T., Shinohara, M., Fujimoto, H., Kanazawa, T., Araya, A., Yamada, T., Iizasa, K.,
680 Tsukioka, S., Omika, S., Yoshiume, T., Mochizuki, M., & Uehira, K. (2018). High-
681 resolution gravity measurement aboard an autonomous underwater vehicle. *Geophysics*,
682 *83*(6), G119–G135. https://doi.org/10.1190/geo2018-0090.1

683 Jamieson, J. W., Clague, D. A., & Hannington, M. D. (2014). Hydrothermal sulfide
684 accumulation along the Endeavour Segment, Juan de Fuca Ridge. *Earth and Planetary*
685 *Science Letters*, *395*, 136–148. https://doi.org/10.1016/j.epsl.2014.03.035

686 Knott, R., Fouquet, Y., Honnorez, J., Petersen, S., & Bohn, M. (1998). Petrology of
687 hydrothermal mineralization: a vertical section through the TAG mound. *Proceedings of the*
688 *Ocean Drilling Program: Scientific Results*, *158*, 5–26.

https://doi.org/10.2973/odp.proc.sr.158.201.1998

Kowalczyk, P. (2011). Geophysical exploration for submarine massive sulfide deposits. *OCEANS'11 - MTS/IEEE Kona, Program Book*. https://doi.org/10.23919/oceans.2011.6107069

Lelièvre, P. G., Carter-McAuslan, A. E., Dunham, M. W., Jones, D. J., Nalepa, M., Squires, C. L., Tycholiz, C. J., Vallée, M. A., & Farquharson, C. G. (2018). FacetModeller: Software for manual creation, manipulation and analysis of 3D surface-based models. *SoftwareX*, *7*, 41–46. https://doi.org/10.1016/j.softx.2018.02.002

Lelièvre, P. G., Carter-McAuslan, A., Farquharson, C. G., & Hurich, C. (2012). Unified geophysical and geological 3D Earth models. *The Leading Edge*, *31*(3), 249–368. https://doi.org/https://doi.org/10.1190/1.3694900

Lelièvre, P. G., & Farquharson, C. G. (2013). Gradient and smoothness regularization operators for geophysical inversion on unstructured meshes. *Geophysical Journal International*, *195*(1), 330–341. https://doi.org/10.1093/gji/ggt255

Lelièvre, P. G., & Oldenburg, D. W. (2009). A 3D total magnetization inversion applicable when significant, complicated remanence is present. *Geophysics*, *74*(3). https://doi.org/10.1190/1.3103249

Li, Y., & Oldenburg, D. (2000). Joint inversion of surface and borehole magnetic amplitude data. *Geophysics*, *65*(2), 540–552. https://doi.org/10.6038/cjg2018L0618

Li, Y., & Oldenburg, D. W. (1998). Separation of regional and residual magnetic field data. *Geophysics*, *63*(2), 791–794. https://doi.org/10.1190/1.1887567

Ludwig, R. J., Iturrino, G. J., & Rona, P. A. (1998). Seismic velocity-porosity relationship of sulfide, sulfate, and basalt samples from the TAG hydrothermal mound. *Proceedings of the Ocean Drilling Program: Scientific Results*, *158*, 313–327. https://doi.org/10.2973/odp.proc.sr.158.225.1998

Murton, B. J., Lehrmann, B., Dutrieux, A. M., Martins, S., de la Iglesia, A. G., Stobbs, I. J.,

715 Barriga, F. J. A. S., Bialas, J., Dannowski, A., Vardy, M. E., North, L. J., Yeo, I. A. L. M.,
716 Lusty, P. A. J., & Petersen, S. (2019). Geological fate of seafloor massive sulphides at the
717 TAG hydrothermal field (Mid-Atlantic Ridge). *Ore Geology Reviews*, *107*(October 2018),
718 903–925. https://doi.org/10.1016/j.oregeorev.2019.03.005

719 Okabe, M. (1979). Analytical Expressions for Gravity Anomalies Due To Homogeneous
720 Polyhedral Bodies and Translations Into Magnetic Anomalies. *Geophysics*, *44*(4), 730–741.
721 https://doi.org/10.1190/1.1440973

722 Parker, R. L., & Huestis, S. P. (1974). The inversion of magnetic anomalies in the presence of
723 topography. *Journal of Geophysical Research*, *79*(11), 1587–1593.
724 https://doi.org/10.1029/jb079i011p01587

725 Petersen, S., Herzig, P. M., & Hannington, M. D. (2000). Third dimension of a presently forming
726 VMS deposit: TAG hydrothermal mound, Mid-Atlantic Ridge, 26°N. *Mineralium Deposita*,
727 *35*(2–3), 233–259. https://doi.org/10.1007/s001260050018

728 Petersen, Sven. (2016). *RV METEOR Fahrtbericht / Cruise Report M127 - Extended Version:*
729 *Metal fluxes and Resource Potential at the Slow-spreading TAG Midocean Ridge Segment*
730 *(26°N, MAR) – Blue Mining@Sea*. *32*(32), 163.

731 Pontbriand, C., & Sohn, R. (2014). Microearthquake evidence for reaction-driven cracking
732 within the Trans-Atlantic Geotraverse active hydrothermal deposit. *AGU: Journal of*
733 *Geophysical Research, Solid Earth*, *120*, 1195–1209.
734 https://doi.org/10.1002/2014JB011376.Received

735 Rona, P. A., Hannington, M. D., Raman, C. V., Thompson, G., Tivey, M. K., Humphris, S. E.,
736 Lalou, C., & Petersen, S. (1993). Active and relict sea-floor hydrothermal mineralization at
737 the TAG hydrothermal field, mid-Atlantic ridge. *Economic Geology*, *88*(8), 1989–2017.
738 https://doi.org/10.2113/gsecongeo.88.8.1989

739 Seyfried, W. E., & Bischoff, J. L. (1981). Experimental seawater-basalt interaction at 300°C, 500
740 bars, chemical exchange, secondary mineral formation and implications for the transport of
741 heavy metals. *Geochimica et Cosmochimica Acta*, *45*(2), 135–147.

https://doi.org/10.1016/0016-7037(81)90157-5

Sharma, P. V. (1997). *Environmental and engineering geophysics*. Cambridge university press.

Shewchuk, J. R. (1996). Triangle: Engineering a 2D quality mesh generator and delaunay triangulator. *Lecture Notes in Computer Science (Including Subseries Lecture Notes in Artificial Intelligence and Lecture Notes in Bioinformatics)*, *1148*(February 1970), 203–222. https://doi.org/10.1007/bfb0014497

Si, H. (2015). TetGen, a delaunay-based quality tetrahedral mesh generator. *ACM Transactions on Mathematical Software*, *41*(2). https://doi.org/10.1145/2629697

Smith, S. E., & Humphris, S. E. (1998). Geochemistry of basaltic rocks from the TAG hydrothermal mound (26°08′N), Mid-Atlantic Ridge. *Proceedings of the Ocean Drilling Program: Scientific Results*, *158*, 213–229. https://doi.org/10.2973/odp.proc.sr.158.218.1998

Szitkar, F., & Dyment, J. (2015). Near-seafloor magnetics reveal tectonic rotation and deep structure at the TAG (Trans-Atlantic Geotraverse) hydrothermal site (Mid-Atlantic Ridge, 26°N). *Geology*, *43*(1), 87–90. https://doi.org/10.1130/G36086.1

Szitkar, F., Dyment, J., Choi, Y., & Fouquet, Y. (2014). What causes low magnetization at basalt-hosted hydrothermal sites? Insights from inactive site Krasnov (MAR 16°38′N). *Geochemistry, Geophysics, Geosystems*, *15*(4), 1441–1451. https://doi.org/10.1002/2014GC005284

Szitkar, F., Petersen, S., Tontini, F. C., & Cocchi, L. (2015). High-resolution magnetics reveal the deep structure of a volcanic-arc-related basalt-hosted hydrothermal site (Palinuro, Tyrrhenian Sea). *Geochemistry Geophysics Geosystems*, *16*(1), 267–300. https://doi.org/10.1002/2014GC005684.Key

Tivey, M. A., Rona, P. A., & Schouten, H. (1993). Reduced crustal magnetization beneath the active sulfide mound, TAG hydrothermal field, Mid-Atlantic Ridge at 26°N. *Earth and Planetary Science Letters*, *115*(1–4), 101–115. https://doi.org/10.1016/0012-821X(93)90216-V

769 Tivey, M. A., Schouten, H., & Kleinrock, M. C. (2003). A near-bottom magnetic survey of the
770 Mid-Atlantic Ridge axis at 26°N: Implications for the tectonic evolution of the TAG
771 segment. *Journal of Geophysical Research: Solid Earth*, *108*(B5), 1–13.
772 https://doi.org/10.1029/2002jb001967

773 Wang, S., Chang, L., Wu, T., & Tao, C. (2020). Progressive Dissolution of Titanomagnetite in
774 High−Temperature Hydrothermal Vents Dramatically Reduces Magnetization of Basaltic
775 Ocean Crust. *Geophysical Research Letters*, *47*(8), 1–11.
776 https://doi.org/10.1029/2020GL087578

777 Wilkens, R. H., Fryer, G. J., & Karsten, J. (1991). Evolution of porosity and seismic structure of
778 upper oceanic crust: importance of aspect ratios. *Journal of Geophysical Research*,
779 *96*(B11). https://doi.org/10.1029/91jb01454

780 You, C. F., & Bickle, M. J. (1998). Evolution of an active sea-floor massive sulphide deposit.
781 *Nature*, *394*(6694), 668–671. https://doi.org/10.1038/29279

782 Zhao, X., Housen, B., Solheid, P., & Xu, W. (1998). Magnetic Properties of Leg 158 cores: the
783 origin of remanence and its relation to alteration and mineralization of the active TAG
784 mound. *Proceedings of the Ocean Drilling Program, Scientific Results*, *158*, 337–351.

785 Zhu, W., Tivey, M. K., Gittings, H., & Craddock, P. R. (2007). Permeability-porosity
786 relationships in seafloor vent deposits: Dependence on pore evolution processes. *Journal of*
787 *Geophysical Research: Solid Earth*, *112*(5), 1–15. https://doi.org/10.1029/2006JB004716

788

789